Atomization of Impinging Opposed Water Jets Interacting With an Air Jet

Yakang Xia, Lyes Khezzar, Mohamed Alshehhi, Yannis Hardalupas(*)

Mechanical Engineering Department, Khalifa University of Science and Technology, Petroleum Institute, Abu Dhabi, United Arab Emirates
(*) Mechanical Engineering Department, Imperial College London, London
Corresponding email address: lkhezzar@pi.ac.ae

Abstract

The characteristics of horizontally opposed water jets in the absence and presence of an impinging air jet are investigated visually with high speed camera and quantitatively using phase Doppler anemometry (PDA). In the absence of air jet, the size of the circular water sheet variation with water jet Reynolds number and Weber number is in agreement with previous findings. The average droplet diameter is found to scale with Weber number and density ratio. Breakup phenomena are captured and described for various combinations of water and air flowrates, which indicate the significant role the air jet plays in promoting water jets atomization. Quantitative measurements using phase Doppler anemometry (PDA) reveals the effects of water flowrates on the generated droplets' size, velocity and root mean square (RMS) distributions and air mass flowrates on the droplets' size distribution along the vertical axis. At various combinations of water flowrates and air mass flowrates, the droplet Sauter mean diameter (D_{32}) along the centerline of the spray, first decreases as a result of the breakup and then increases slight possibly due to the coalesce of droplets or preferential dispersion of different droplet sizes after break was complete. Larger water flowrates result in larger D_{32}, while larger air mass flowrates lead to smaller D_{32} values. Variation of D_{32}/d, where d is the pipe diameter, against the air liquid momentum ratio reveals that the horizontally opposed impinging jet arrangement leads to better atomization than the one with liquid jet impingement angle of 90°.

Key words: Opposed impinging liquid jets; atomization; PDA; droplet size; droplet velocity

1. Introduction

Liquid impinging jets are utilized in a variety of industrial processes involving mixing, precipitation of micro or Nano-particles, and atomization such as in liquid propellant rocket engines [1-4]. Their benefits include manufacture simplicity, excellent mixing rate and atomization performances [5]. The present paper documents an experimental study of the behavior of two liquid horizontally impacting opposed jets in the absence and presence of an impinging third vertical air jet to gain better understanding of atomization behaviors.

Generally, when two round liquid jets of same momentum and diameter collide with each other, an expanding liquid sheet bounded by a thicker rim appears in the plane perpendicular to the plane where the two jets are located. Interest in this configuration goes far back with the pioneering observations of Savart [6], who identified the breakup of the flat sheet. If the two jets are oblique and impinge with each other at an angle less than 180°, the liquid sheet shape is elliptical and leaf-like [7-9], whereas a circular sheet is generated [10] when the two jets are opposed to each other and share the same axis. In both cases, under the influence of surface tension, inertial, viscous and aerodynamic forces, the resultant sheet is subject to disturbances that lead to its disintegration in the form of ligaments and droplets [11].

Oblique impinging jets for laminar and turbulent flow and for Newtonian and non-Newtonian fluids have received considerable attention and their behaviors in terms of mechanisms of atomization, including visualization of breakup phenomena, breakup regimes, sheet thickness and droplet size measurement have been documented in a number of studies [7-9, 12-16].

Opposed liquid jets were studied by Huang [17], who identified the different regimes associated with the behavior of the circular liquid sheet, its stability and radial extent. Circular smooth and flapping sheets generated using a slender liquid jet impacting a solid disc were the subject of studies by Villermaux and Clanet [18, 19] who studied the radial extent of the sheet and the mean generated droplet size.

Additional studies [2, 10, 20-25] of opposed colliding liquid jets were concerned with rapid mixing properties of two impinging streams and the stability of the stagnation plane or point as this configuration forms the basis of the free impinging jet reactor. In this instance the stagnation plane location and behavior and its velocity field and turbulence content play an important role in scalar mixing where diffusion scales are increased [10]. Li, et al. [23] pointed out that stagnation point offset caused by exit momenta difference is found to be the principal

instability regime, and that it can be reduced by increasing exit turbulent intensity and a uniform exit velocity profile, but it is impossible to get the impingement stagnation point to remain at the mid geometrical point. Icardi, et al. [2] investigated twin liquid opposed jets in a confined impinging jets reactor at low flowrates corresponding to jet exit Reynolds number defined by the fluid density, viscosity, mean velocity and inlet pipe diameter range from 62 to 600 using PIV (Particle Induced Velocimetry) and DNS (Direct Numerical Simulation). It was found that eddies of different sizes generated from the breakup of the impingement plane enhance turbulence and mixing. Zhang, et al. [10] measured the average diameter of the liquid impingement plane and velocity statistics using PIV. The diameter of the liquid circular sheet was found to increase linearly with Reynolds number in the range of 1800 to 4100, and the turbulence kinetic energy (TKE) increases with jet velocity and decreasing distance between the two liquid jet nozzle exits. Stagnation point location was found to be non-sensitive to Reynolds number changes. Zhang, et al. [21] also measured velocity fluctuations, turbulent intensity and TKE in the impinging jets with laser Doppler anemometry. Turbulent intensity and TKE were found to decrease with increasing nozzle diameter and increase with liquid flowrates. On the numerical side, Wu, et al. [24] simulated the behavior of the stagnation plane generated from two turbulent opposed jets with DNS. Zhang, et al. [25] conducted an investigation about a novel free triple-impinging jets atomizer with PIV, which is made by adding an extra liquid jet to the opposed jets. Velocity distribution and turbulent kinetic energy were analyzed in terms of the effects of Reynolds number and jet spacing.

Enhanced atomization from two impinging liquid jets by adding a third micro air jet that impacts the other two jets at the impingement point has been documented by Avulapati and Venkata [26]. The effects of liquid viscosity, surface tension and gas to liquid ratio were investigated. The results proved that viscosity influenced the atomization more than the surface tension. Xia, et al. [27] investigated the velocity and droplet characteristics of two oblique liquid jets impinged upon by an air jet and found that the air jet promotes atomization to a great extent.

The case of two opposed liquid horizontal jets interacting with a third vertical air jet has not been studied in detail previously and so the present study intends to fill this gap. The objective of the current study is to investigate the atomization behavior of such a configuration and extend the previous work of Xia, et al. [27]. Flow visualization is conducted using high speed camera to provide qualitative and quantitative description of the flow with and without an air jet. Droplets'

size and velocity distributions are measured with phase Doppler anemometry (PDA) to provide detailed information on the downstream droplets' flow behavior in the near field.

2. Experiment

Water and air were chosen as working fluids and the experiment was conducted at atmospheric pressure and an ambient room temperature of 20 ºC. Flow visualization using high speed photography and droplet size and velocity measurements with PDA are used in the experimental program.

2.1 Experimental setup

Fig. 1 presents the schematic of the experimental setup consisting of a water and air supply system to the atomizer, and the optical setup, including the high speed camera and PDA, for the measurement of the spray characteristics. In the water and air supply, water stored in a tank is supplied to the liquid jet nozzles using two magnetically coupled centrifugal pumps, and then returns to the tank after exiting the nozzles. The water flowrate is controlled by two needle valves and measured with two calibrated Omega water flow meters with an accuracy of 1%. Air from a centralized compressed air supply system is supplied to the air jet nozzle and the air flowrate is measured by an Alicat mass flow meter with an accuracy of ±0.3% reading +0.2% F.S. A K-type thermocouple is inserted into the water tank to monitor the water temperature throughout the experiment to ensure that there is no significant variation in temperature to avoid affecting fluid viscosity and hence the atomization performance. The flow visualization set up includes a FASTCAM SA3 high speed camera, together with an LED matrix, providing back illumination to capture the two-phase flow behavior. Quantitative measurements of droplets' size and velocity information were conducted using a 2D TSI PDA system, which consists of an Argon-Ion laser, transmitting optics, receiving optics, photo detector module (PDM) and multi digital processor (MDP).
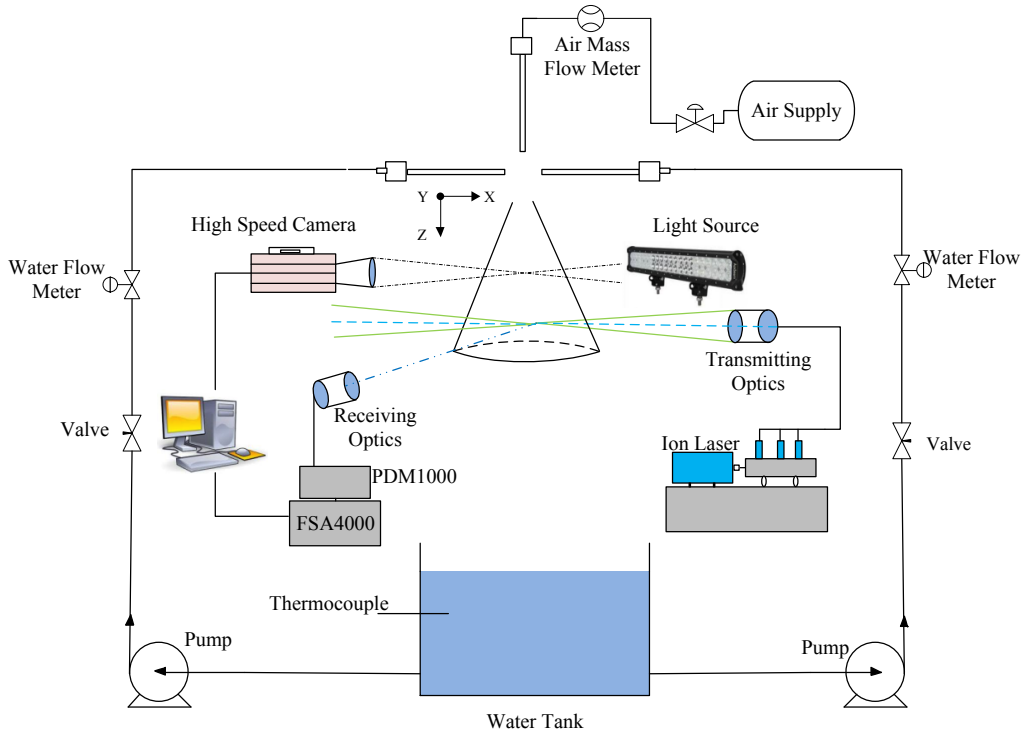
Fig. 1. Schematic of experiment setup

The schematic of the impinging jets atomizer is shown in Fig. 2, which consists of three stainless steel pipes with an equal internal diameter d = 1.0 mm. The water pipes are 152.4 mm in length, resulting in a length to diameter ratio L/d = 152.4, while the air pipe was 304.8 mm, L/d = 304.8, leading to fully developed conditions at the exit of both air and liquid nozzles. A manufactured well aligned frame is used to hold the three pipe-nozzles in place. The distance between the nozzle exit and the geometrical impingement point O is 10 mm. The atomizer is fixed onto a three-dimensional computer-controlled traverse system from TSI. The positional accuracy of the traverse system is 0.01 mm. The geometrical impingement point O is the reference point (0, 0, 0) in the XYZ coordinate system shown in Fig. 2. The YZ plane (i.e. X = 0 mm) is referred as water sheet plane.

2.2 Flow visualization technique

With the high speed camera, and background illumination, images were captured from two directions (30° view and side 90° view with respect to the water jet axis, see Fig. 3). They were then analyzed using the software Photron Fastcam Viewer Ver.352 and captured at frame rates of 15,000 fps and 20,000 fps for far and near-field respectively, corresponding to resolution of 256×256 and 512×128 pixels leading to spatial resolution of 0.211 mm/pixel and 0.165 mm/pixel

respectively. The sequence of instant camera photographs allows observations of temporal and spatial variations of the flow structure. For the case where the air jet is absent, the average diameter of the generated water sheet has been measured using 50 frames with a public domain, Java-based image processing program ImageJ developed at the National Institutes of Health [28, 29] with uncertainties less than 5% of the averaged diameter.
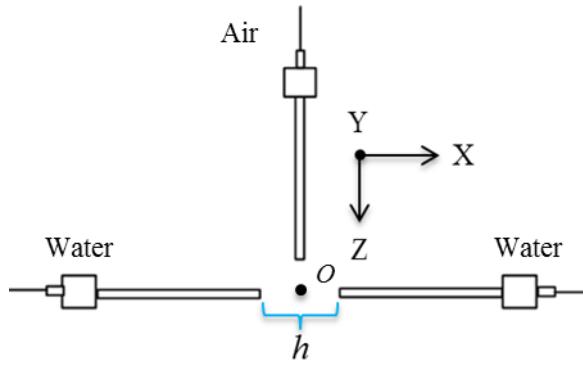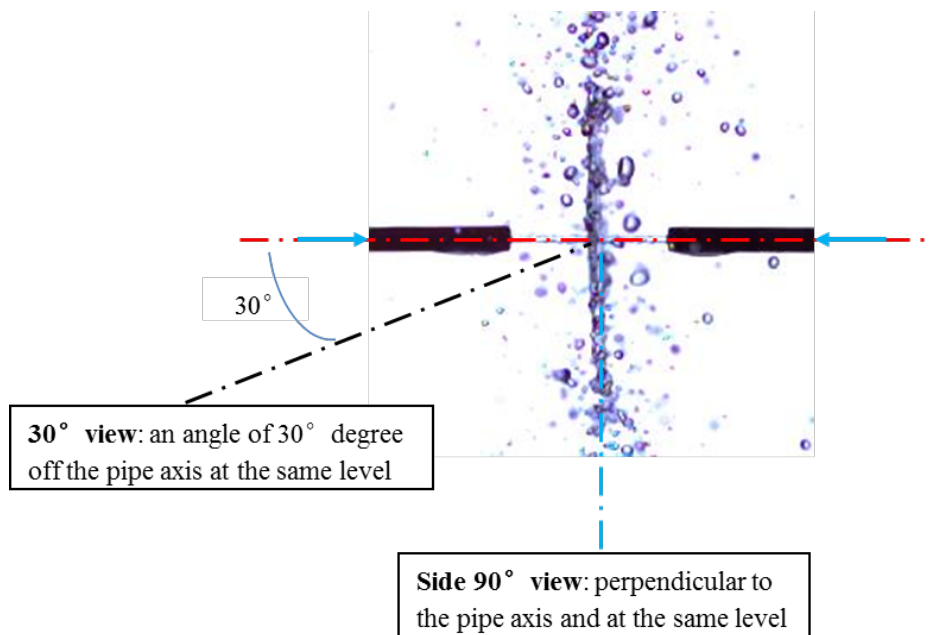

Fig. 2. Structure of atomizer

Fig. 3. Definition of different views of observation

2.3 PDA technique

The 2D PDA system consists of an air-cooled Argon-ion laser, a TSI450401 transmitter probe with a XPD50-E expander, a TSI 450305 receiver a photomultiplier PDM1000 (Photo

Detector Module), and a FSA4000 multi-bit digital signal processor. With the Flow-Sizer software, the velocity of the droplet is obtained in the same way as in a laser Doppler anemometer from the frequency of the light intensity fluctuations based on the proportional relationship among light intensity frequency, fringe spacing and velocity. Droplet's size information is obtained from the phase shift between two Doppler signals converted from the optical signals captured by the photo-detectors positioned at different angles [30].

In this study, an L-shape frame is utilized to support and fix laser transmitter and receiver to achieve good and easy alignment. The systematic accuracy for droplet size measurement is less than $1\%D_{max}+1\%D_{measurement,}$ and repeatability is 0.5%, while for velocity it is less than 0.2% and repeatability is 0.05% [31]. The statistical uncertainties for droplet size and velocity averaged values are about 2% and 1% respectively based on statistics from 10,000 samples. The overall uncertainty of the droplet Sauter mean diameter is estimated to be $\pm$4%, and droplet velocity $\pm$ 1%.

2.4 Experimental conditions

The experimental conditions are listed in Table 1. Flow visualization was carried out firstly without the air jet, and then the effects of air mass flowrate were evaluated by using different air mass flowrates of $\dot{m}_g$ = 5.7, 11.4, 22.8 g/min.

Table 1. Experimental conditions

Water flowrate (single jet) Q_L(mL/min)	100-250			
Air mass flowrate $\dot{m}_g$ (g/min)	5.7	11.4	17.1	22.8
h/d	20			

Quantitative measurements along the Y-axis at a location of 75 mm below the impinging point and along the Z-axis were conducted respectively to study the effects of water and air mass flowrates. Measurements on the water sheet plane (X = 0 mm) were also obtained in terms of spatial distributions of droplet size and velocity.

3. Results

In this section, a qualitative description of the flow of impinging jets without and with an air jet using flow visualization is presented first. These include the variation of the diameter of the liquid sheet with Reynolds and Weber numbers in the absence of an air jet and discussion of

atomization without and with the air jet. Quantitative information from measurements of droplet size, mean velocity and RMS of velocity fluctuations are presented next.

3.1 Flow visualization

Fig. 4 displays instantaneous images (30° view and side 90° view) of the water sheet that is generated by two coaxial opposed impinging jets having the same flowrate but in the absence of an air jet, i.e. in still surrounding air. The liquid flowrate varies from 100 to 250 mL/min. Images on the left are taken at an angle of 30° off the liquid jet axis, while images on the right side are taken from the side perspective, which corresponds to 90° view. A circular liquid sheet is generated at the stagnation point of the two liquid streams. For flowrates between 100 and 125 mL/min, the generated water sheet is very smooth and possesses a thicker rim from which a small number of relatively large diameter water droplets are shed. At higher flowrates, starting from 150 mL/min the diameter of the liquid sheet increases and disturbances in the form of circular transverse waves originating from the stagnation point and travelling towards the rim can be seen on its surface. The liquid sheet surface becomes blurred as can be seen by observing the pipe behind it. These waves propagate towards the rim, where now in addition to droplets ligaments can be seen. For flowrates higher than 150 mL/min, the water sheet loses its circular shape randomly around the circumference and intermittently with time by losing some parts of its area, which are torn away and disintegrate into a range of droplet sizes. It is found that droplets become smaller with increasing water jet velocity and this is clearly shown for $Q_L = 225$ mL/min. For even higher flowrates, around 200 mL/min, the liquid sheet oscillates with low amplitudes around its central or stagnation vertical plane. This type of large scale instability has been reported previously by Li et al. [23] and Wu et al. [24], and has been found to be due to a vortex ring located at the impingement zone, which is responsible for the time-dependent axial movement of the stagnation point.
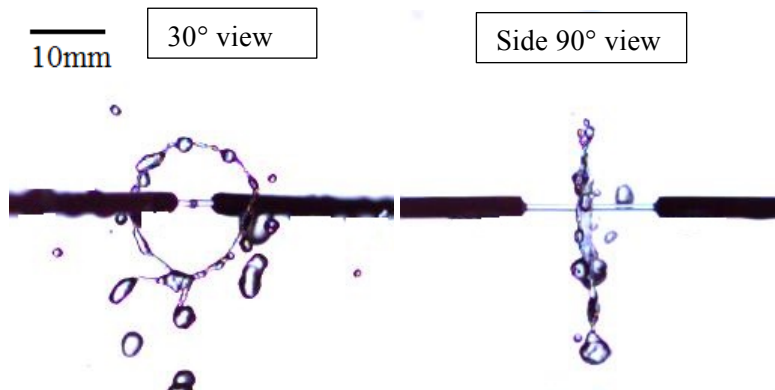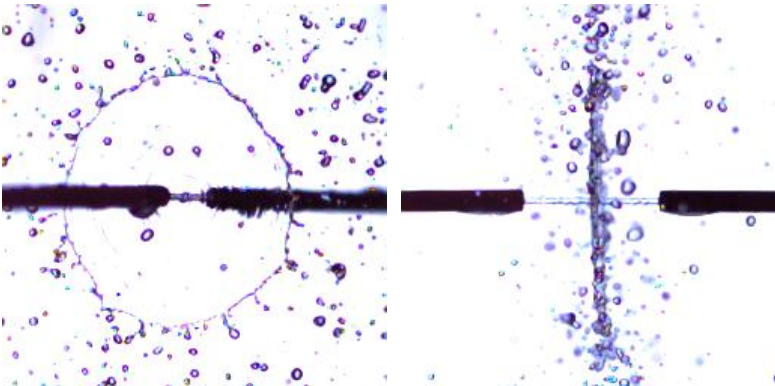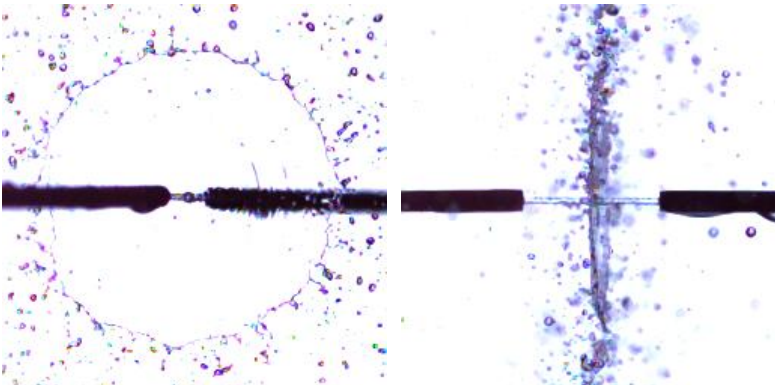
Q$_L$ = 100 mL/min (*Re* = 2114; *We* = 62)

Q$_L$ = 125 mL/min (*Re* = 2642; *We* = 96)
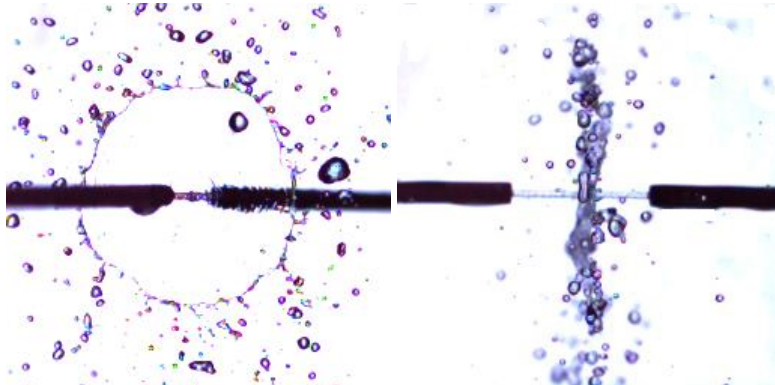
Q$_L$ = 150 mL/min (*Re* = 3170; *We* = 139)

Q$_L$ = 175 mL/min (*Re* = 3699; *We* = 189)

Q$_L$ = 200 mL/min (*Re* = 4227; *We* = 247)

Part of the water sheet being torn apart and disintegrating.

Q_L = 225 mL/min (Re = 4756; We = 313)

Q_L = 250 mL/min (Re = 5284; We = 386)
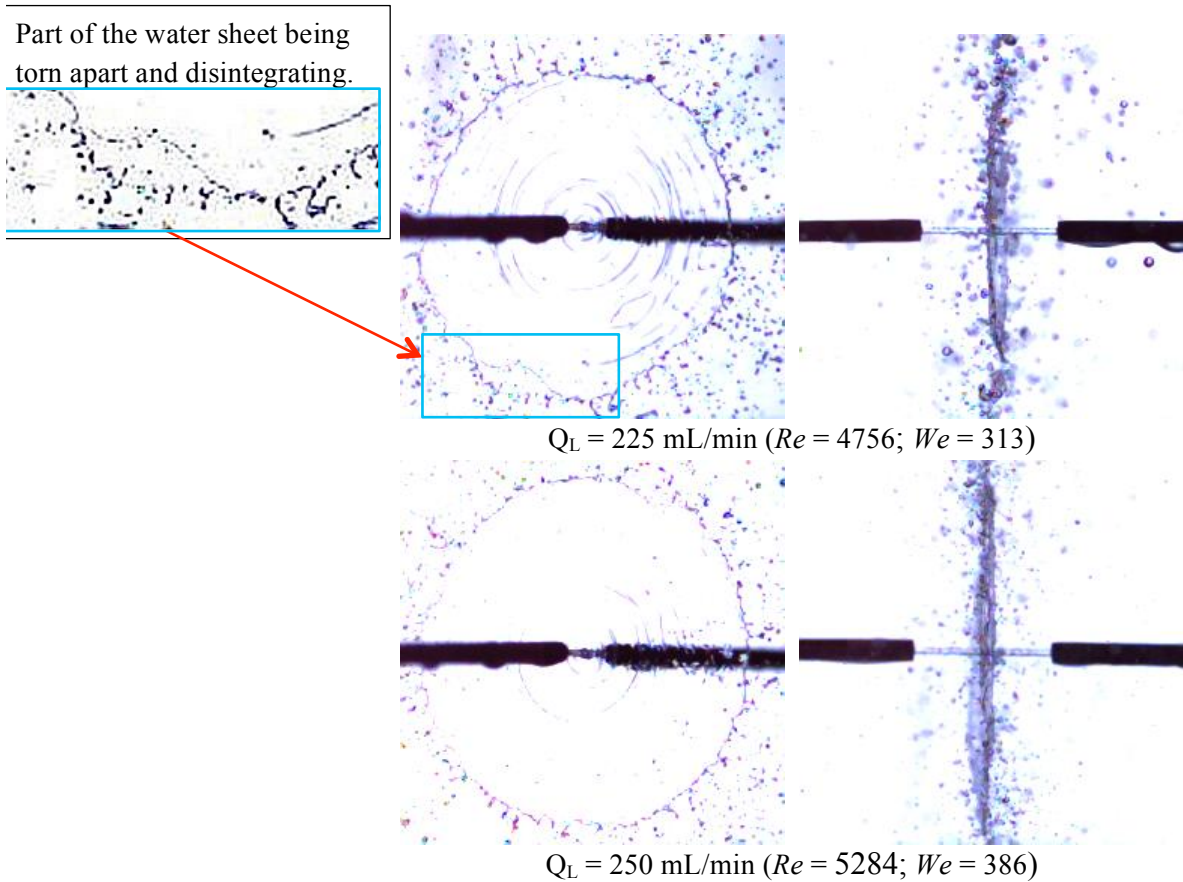
Fig. 4. Images of water sheet generated by opposed jets at h/d = 20

The average diameter of the impingement water sheet is shown in Fig. 5 for a range of Re and two values of nozzles' distances of h/d = 10 and 20. The Reynolds number is defined by the fluid density ρ_l, viscosity μ_l, mean velocity U_l and pipe diameter d as in equation (1). It can be seen that the diameter increases almost linearly with increasing Reynolds number in a similar fashion as observed in [10]. However, in the current study, the difference between results from the two different nozzle distances used is not perceptible.

$$Re = \frac{\rho_l d U_l}{\mu_l} \qquad (1)$$
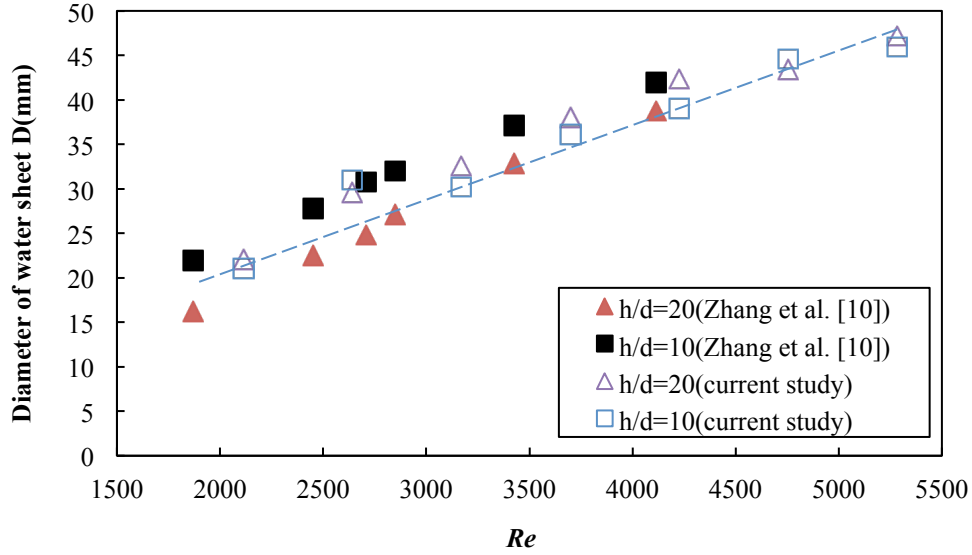
Fig. 5. Water sheet diameter against the water jet Reynolds number *Re*. Lines are just for visual aid.

It has been previously established that depending on the liquid jet Weber number, a horizontal liquid sheet may undergo several regimes [17, 18, 32]. The Weber number (*We*) is defined by density of fluid ρ_l, surface tension of liquid σ_l, mean velocity at the pipe exit U_l and pipe diameter *d* as in equation (2). Starting with a stable regime for $100 < We < 500$, it moves to a transition regime for $500 < We < 1000$ and reaches an unstable regime for $We > 1000$, where antisymmetric waves appear on the liquid sheet and this later starts to flap with a flag like motion. In the stable regime, a semi-empirical relationship between D/d and *We* was derived [18, 32]. Thus, for this experiment, evolution of the water sheet diameter D/d presented as a function of the water jet Weber number is shown in Fig. 6, together with the relationships of Huang [17] and experimental results of Clanet [32] and Villeurmaux and Clanet [18, 19]. Fig. 6 uses the scaling relationships between $(\alpha^{1/2} We\ \mathrm{D/d})\ (\alpha^{1/2} We)^{1/3}$ and $\alpha^{1/2} We$ that introduce the *We* and density ratio α. It can be seen that, for the *We* range covered by the experiments, D/d increases almost linearly with increasing $\alpha^{1/2} We$. The present results display larger values than both previous studies below $\alpha^{1/2} We = 5$ and fall within the previous range results beyond that value.

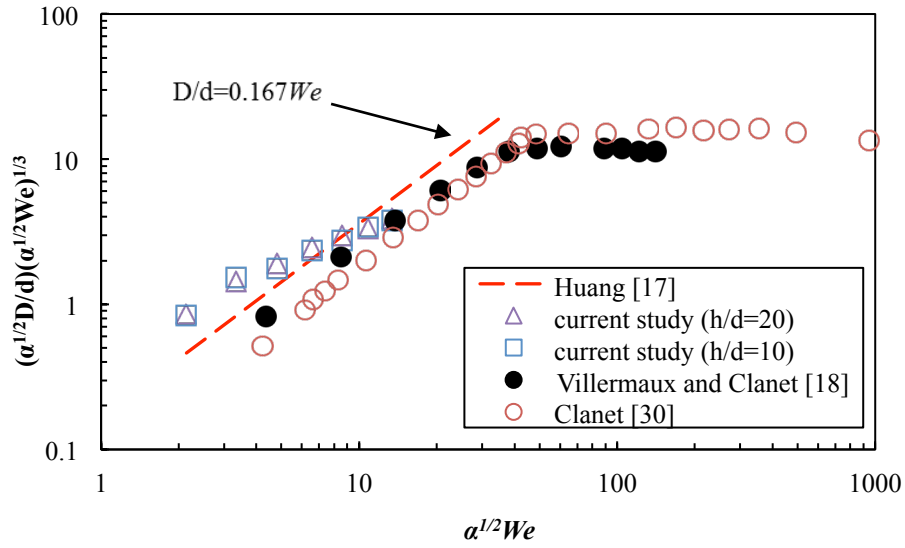$$We = \frac{\rho_l U_l^2 d}{\sigma_l} \qquad (2)$$

11

Fig. 6. Sheet diameters dependence on the Weber number and density ratio
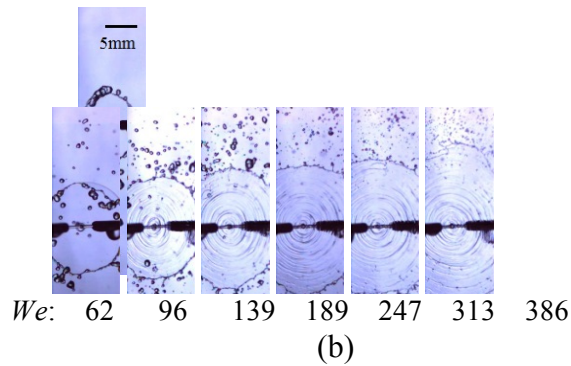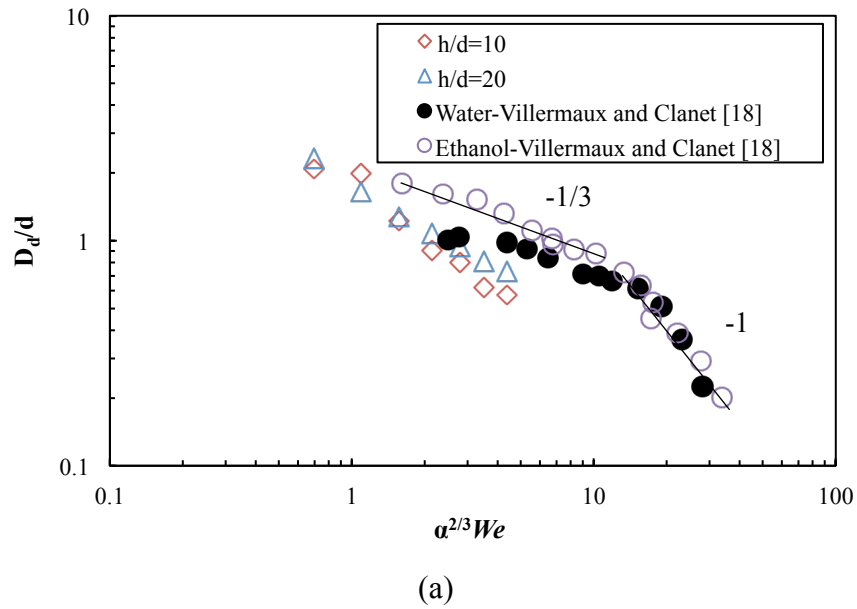

(a)

(b)

Fig. 7. (a) Droplet mean diameter against $\alpha^{2/3}We$. Lines are just for visual aid. (b) Photos for droplet size measurement

Fig. 7 (a) displays the mean droplet diameter (D_d) normalized with the nozzle diameter against the scaled Weber number $\alpha^{2/3}We$. The liquid nozzle diameter in [18] was equal to 2.7 mm, whereas in the present experiments it is 1.0 mm. The droplet diameters are measured from the occupied area by each droplet on the images as in Fig. 7 (b), using the software ImageJ. The droplet diameter results of Fig. 7 are estimated from 300 droplet samples from a sequence of representative images chosen from a total number of 1000 images. Overall uncertainty of the mean droplet diameter combining both systematic error (caused by spatial pixel resolution) and standard deviation of the fluctuations of the droplet diameter is around 25% of the mean values, which is of the same order as those in [19]. It can be seen that the present results extend the range of previous measurements and correlate with the previous findings, although relatively smaller values were measured within the range of the scaling variable $\alpha^{2/3}We$ between 3 and 5. Results from [18], presented in Fig. 7 (a), also suggest that to reach a mean droplet size around 100 μm a value of We of 6000 is necessary, which, for this case, would necessitate a high liquid jet momentum. To improve on the atomization, and at the same time avoid the difficulty in providing water jets of high velocities, an extra air jet issuing from a pipe of the same size with that of the water jet is added to the existing coaxial opposed impinging jets, as shown in Fig. 2. The effects of the air jet on opposed water jets atomization are described qualitatively for liquid volume flowrate $Q_L = 175$ mL/min and three different air mass flowrates of 5.7, 11.4 and 22.8 g/min.

$\dot{m}_g = 5.7$ g/min
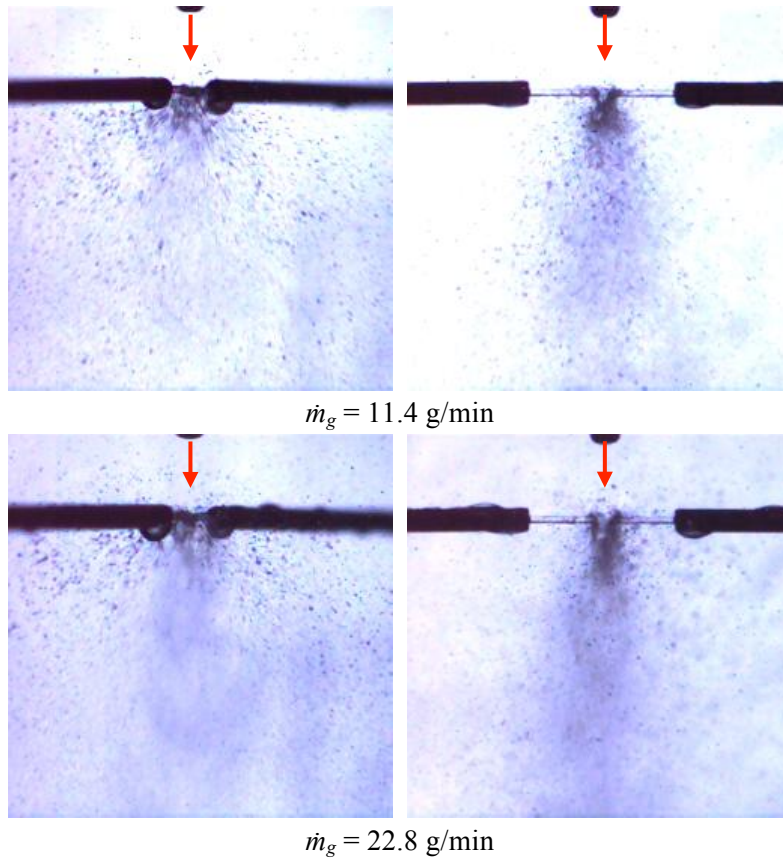
$\dot{m}_g = 11.4$ g/min
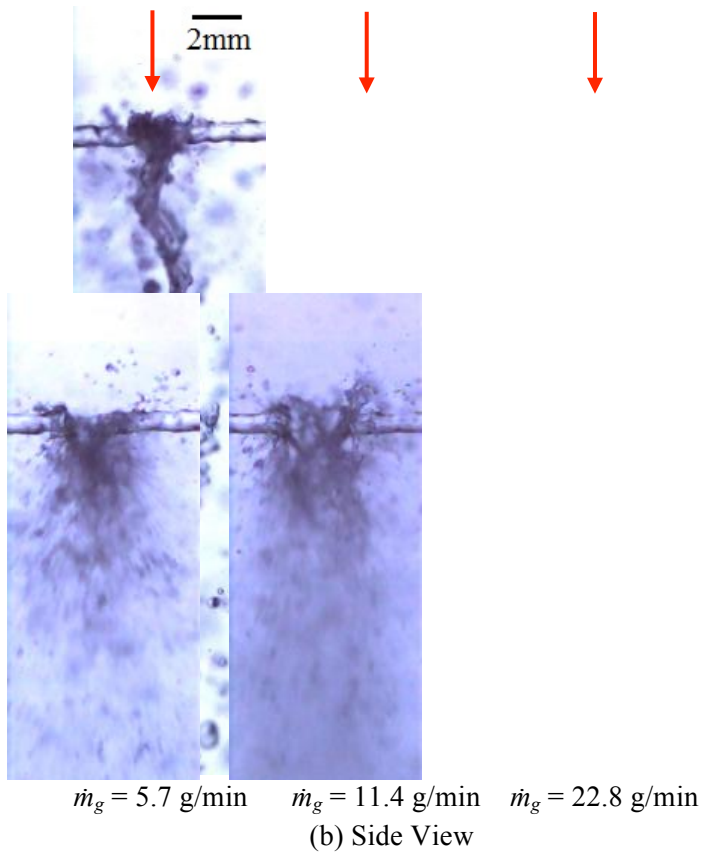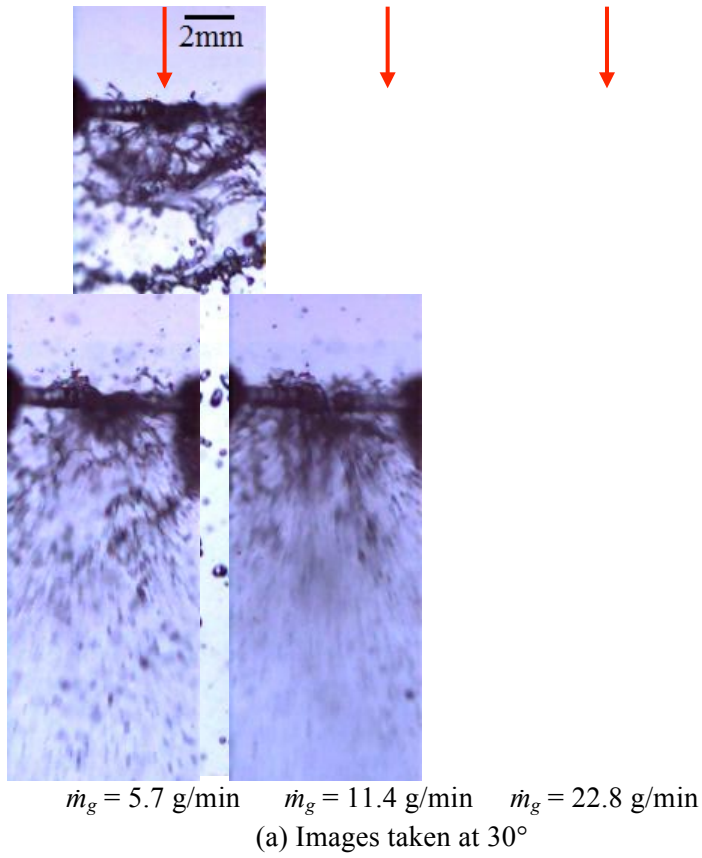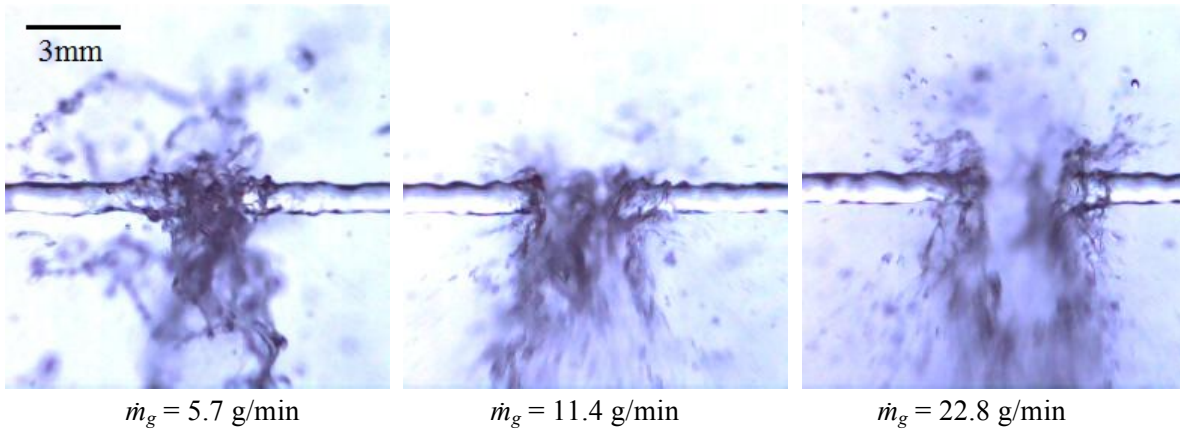
$\dot{m}_g = 22.8$ g/min
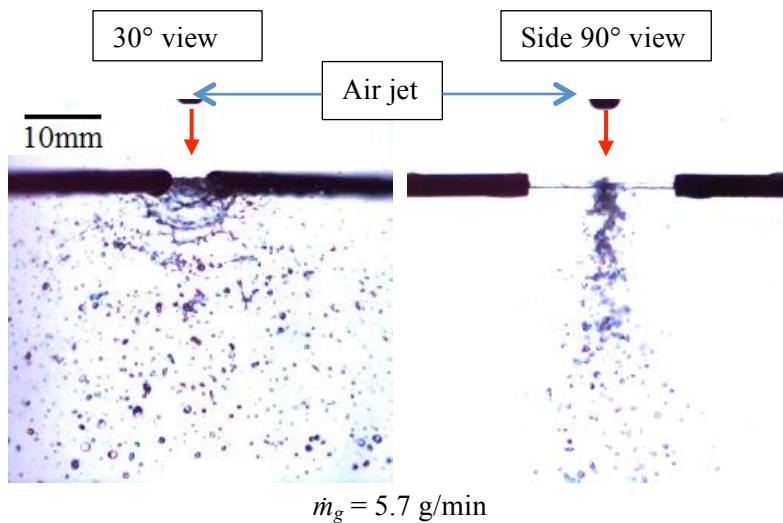
Fig. 8. Images at various air mass flowrates at $Q_L = 175$ mL/min (Re = 3699)

As shown in Fig. 8 and Fig. 9, for $\dot{m}_g = 5.7$ g/min, the water sheet above the plane of the pipes totally disappears, while in the region below the impingement point, arc shaped ripples in the water sheet are generated periodically from the impingement point, which then expand radially and give rise to ligaments and droplets through bag break up mechanisms [33]. Judging from the side view images, the displayed waviness is in the direction of the water pipes. Increasing the air mass flowrate to 11.4 g/min, from the close image in Fig. 9, one can see a finer spray with only the existence of patches of stretched ligaments, and, as shown in Fig. 8, in the downstream region, water is totally atomized into small droplets. Further increasing $\dot{m}_g$ to 22.8 g/min, generated much smaller droplets. One sees in Fig. 9 (c) that the two liquid jets cannot reach each other as the air jet penetrates deep into the stagnation region. In this instance, ligaments and droplets are peeled out from the tip of the water jet, and entrained downstream.

$\dot{m}_g$ = 5.7 g/min $\dot{m}_g$ = 11.4 g/min $\dot{m}_g$ = 22.8 g/min

(a) Images taken at 30°

$\dot{m}_g$ = 5.7 g/min $\dot{m}_g$ = 11.4 g/min $\dot{m}_g$ = 22.8 g/min

(b) Side View

$\dot{m}_g = 5.7$ g/min $\dot{m}_g = 11.4$ g/min $\dot{m}_g = 22.8$ g/min

(c) Images taken from upside perspective

Fig. 9. Close images at various air mass flowrates at $Q_L = 175$ mL/min

3.2 PDA measurement results

In this section detailed quantitative data on droplet size and velocity measurements from the PDA system are illustrated in terms of spatial distribution, effects of liquid and air flowrates.

- **Spatial distribution of droplet size and velocity on the plane X = 0 mm**
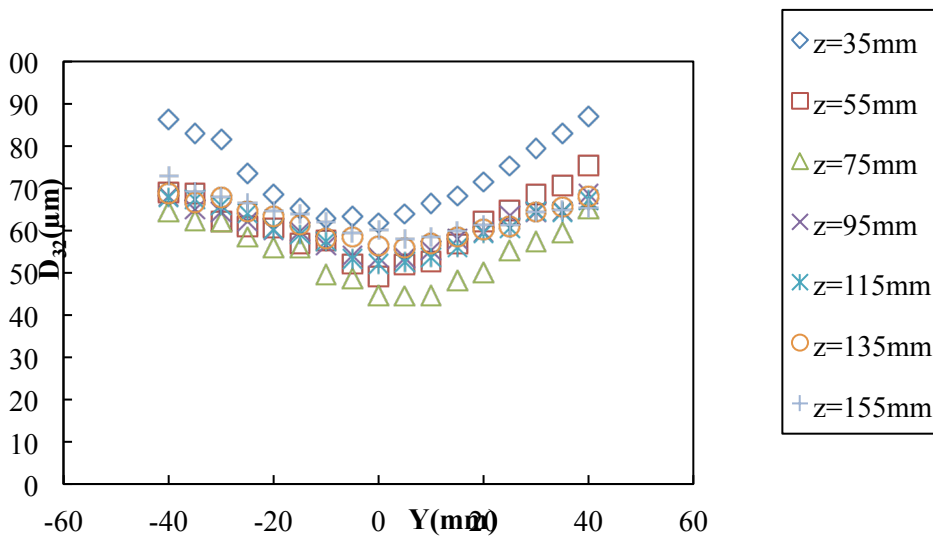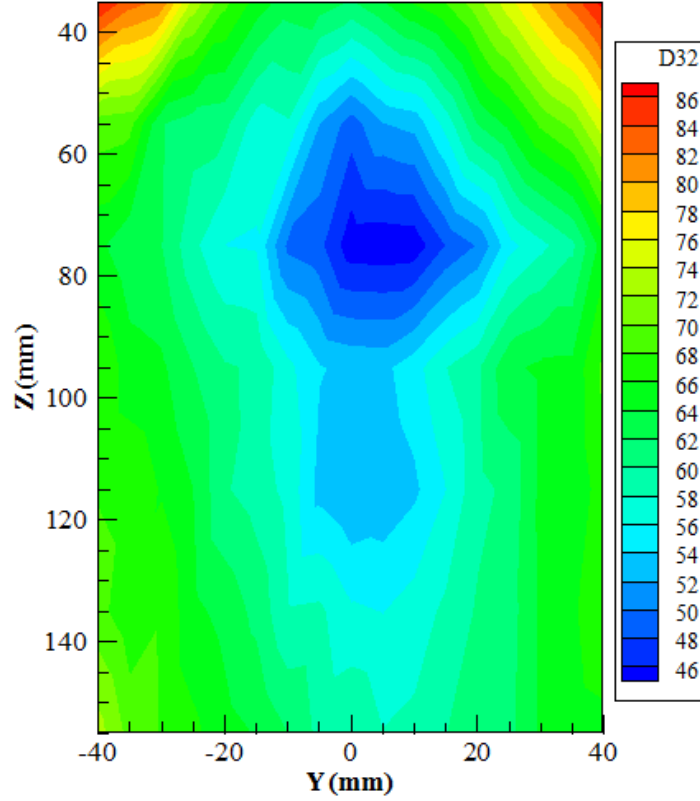
Fig. 10. D_{32} (μm) distribution at Q_L = 175 mL/min and $\dot{m}_g$ = 11.4 g/min

Sauter mean diameter (D_{32}) profiles on the water sheet plane X = 0 mm for $\dot{m}_g$ = 11.4 g/min and Q_L = 175 mL/min is displayed in Fig. 10. Measurements were taken along the Y-axis at different axial locations from Z = 35 mm downwards from the impinging point up to Z = 155mm. D_{32} is smallest in the central part of the flow field and increases towards the edges of the spray. As we move along the Z-axis, the droplet size firstly decreases from 62 μm at 35 mm to 44.7 μm at Z = 75mm with the occurrence of first and secondary breakup [33], and then increases again due to coalescence of small droplets or preferential dispersion of different droplet sizes after the complete breakup to reach 60 μm at Z = 155 mm. The contour figure of D_{32} spatial distribution in Fig. 10 more clearly indicates that the smallest droplets exist in the spray central region around 75 mm downstream the impingement point.
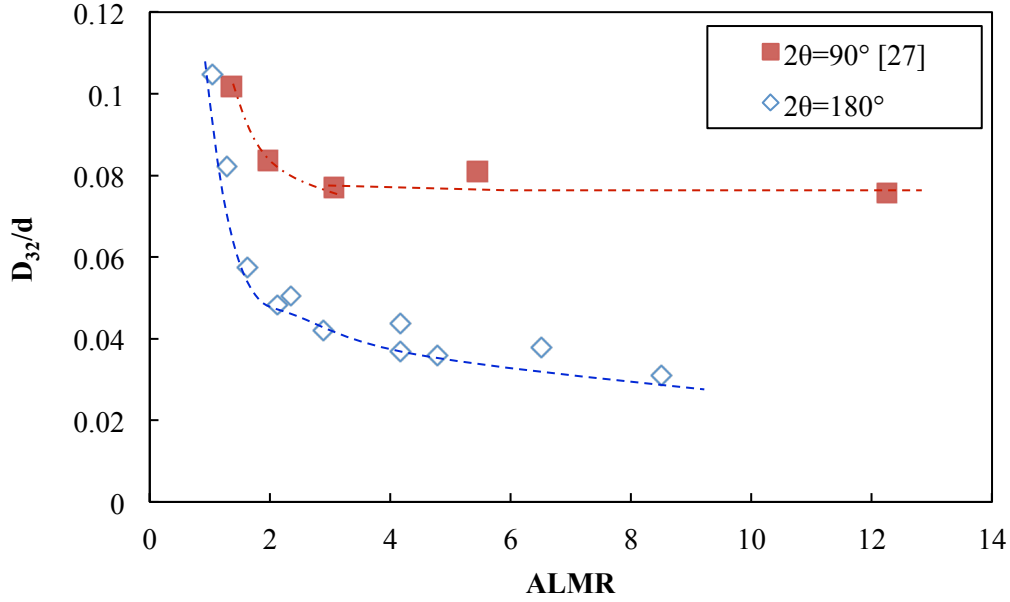
Fig. 11. Variation of non-dimensional SMD with air to liquid momentum ratio ALMR (open symbol represents the data from current study, closed symbol stands for 2θ = 90° by Xia, et al. [27])

To eliminate the effect of air jet diameter, a non-dimensionalized SMD with the air jet pipe diameter is depicted in Fig. 11 against the air to liquid momentum flux ratio ALMR, which is defined in equation (3) [34]. D_{32}/d decreases rapidly from a value of 0.1 to reach an almost constant value of around 0.04 at an ALMR value of 4. Comparison between the cases of water jets impingement angle 2θ = 90° for an oblique configuration [27] and opposed axial impinging water jets indicates that a larger impinging angle provides improved atomization. This statement is of course based on the measurements of D_{32} along the centerline in the impingement plane (X = 0 mm).

$$ALMR = \frac{\dot{m}_g U_g}{\dot{m}_l U_l} \qquad (3)$$

(a)

(b)
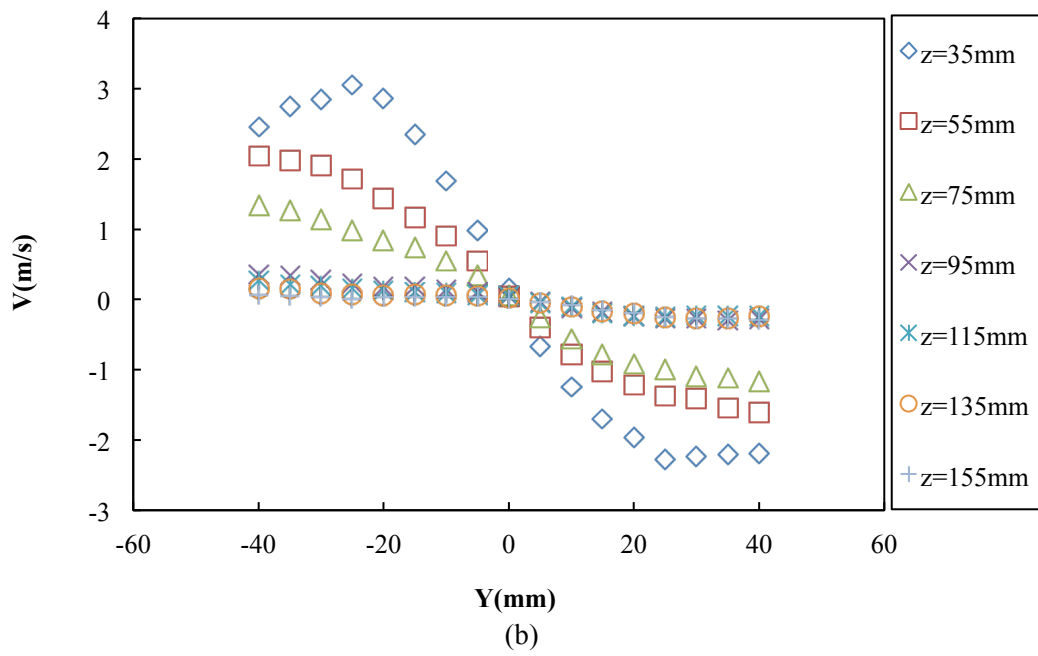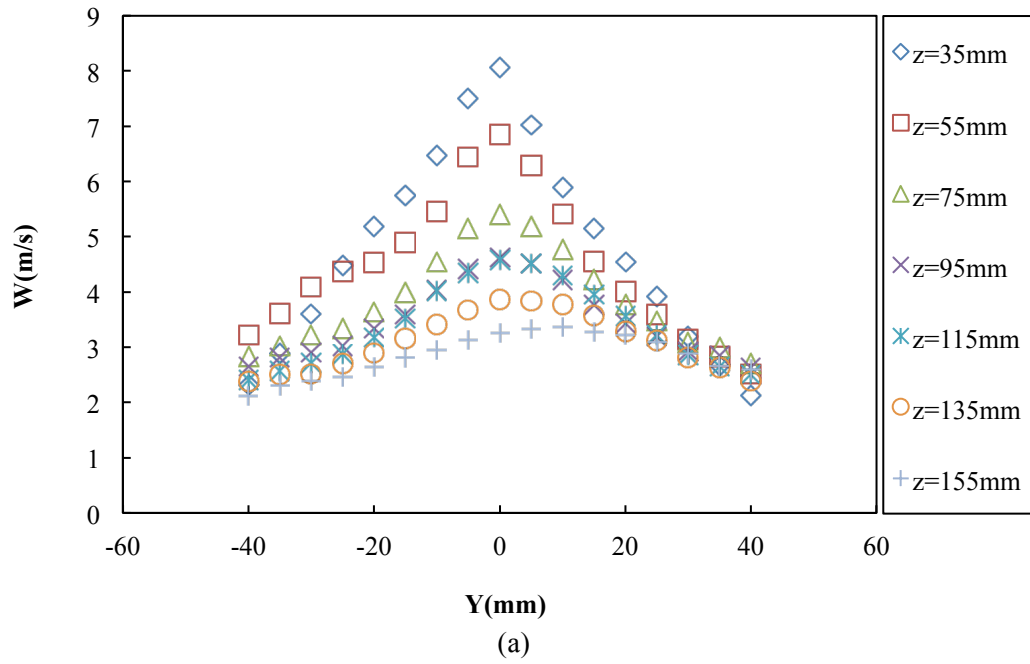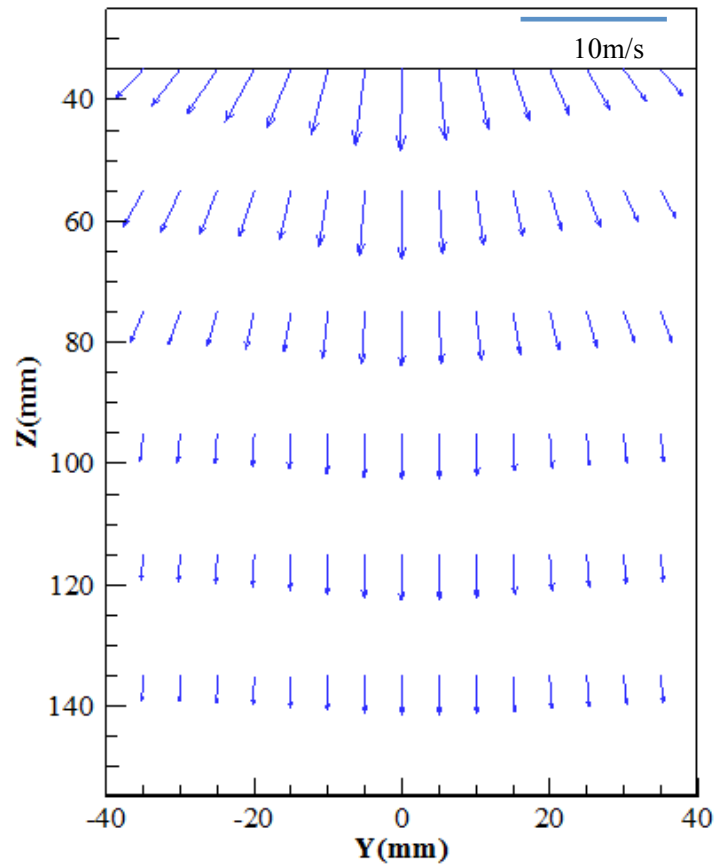
(c)

Fig. 12. Droplet velocity distribution: (a) axial component W; (b) radial component V; (c) velocity vector

Droplet velocity data includes mean axial and radial velocity components and their root mean square (RMS) of the velocity fluctuations. Fig. 12 presents the mean axial velocity component W, radial velocity component V and the velocity vector generated from the two components in the water sheet plane X = 0 mm. The axial velocity profiles are modulated by the air jet profile with a bell shaped curve having its maximum in the center and gradually decreasing towards the edges of the spray, while radial velocity shows an opposite trend where the magnitude of the radial velocity is the smallest (V = 0 m/s) in the spray center and increases outwards. From the velocity vector, it is easy to notice that droplets travel downwards and outwards.

Profiles of the RMS of velocity fluctuations of the W component are shown in Fig. 13 (a). The profiles display large values in the central part and lower values towards the spray edges. At downstream locations, the RMS values decrease to display a uniform profiles at Z = 155 mm. This trend indicates a decrease in droplet velocity fluctuations. In contrast, the profiles of the RMS of the radial velocity fluctuations, see Fig. 13 (b), show low values in the central part that

increase at large radial positions, in the vicinity of the impinging point. The profiles tend to flatten with low values and become uniform with downstream distance. There are two possible reasons why the RMS of the radial velocity fluctuations increases away from the vertical axis. First the droplet size distributions are wider at large distances from the spray axis than at the region close to the spray axis, as the droplet histograms show in Fig.14 (a) and (b). This is also verified by the increased Sauter mean diameter of Fig. 10 at large distances from the axis, which happens because of the increased number of large droplet sizes being present at these locations. The droplet velocities vary with droplet size and the size-velocity correlation in Fig.15 (b) indicates that the small and large droplets move with a wider range of velocities at these locations in the spray. As a consequence, since the presented velocity is averaged over all droplet sizes, the corresponding velocity probability function of all droplets becomes wider, since it combines the velocities of small and large droplets. Therefore, the RMS of the droplet velocity fluctuations increases at these locations. As the axial distance from the impingement point increases (e.g. at Z=75mm), further breakup occurs, see Sauter mean diameter of Fig. 19. As can be seen from Fig. 15 (c) and (d), the size-velocity correlation weakens and, as a consequence, small and large droplet sizes move with similar velocities leading to narrower velocity probability functions, and lower RMS of velocity fluctuations. The second reason is related to the ballistic trajectories of the large droplets, which do not respond to the air flow due to their large inertia. As a consequence, droplets, generated at different locations during the breakup of the liquid, have different original velocities and can travel over a long distance along the ballistic trajectories. This behavior of inertial droplets has been termed 'fan-spreading effect'[35] and leads to droplets reaching at the same location in space from a long distance and with different initial velocities which are maintained due to lack of response to the air flow. The final outcome of this effect is to broaden the local droplet velocity probability functions and increase the resulting RMS of the droplet velocity fluctuations and has been observed for droplets in swirling flows (e.g. [36]).
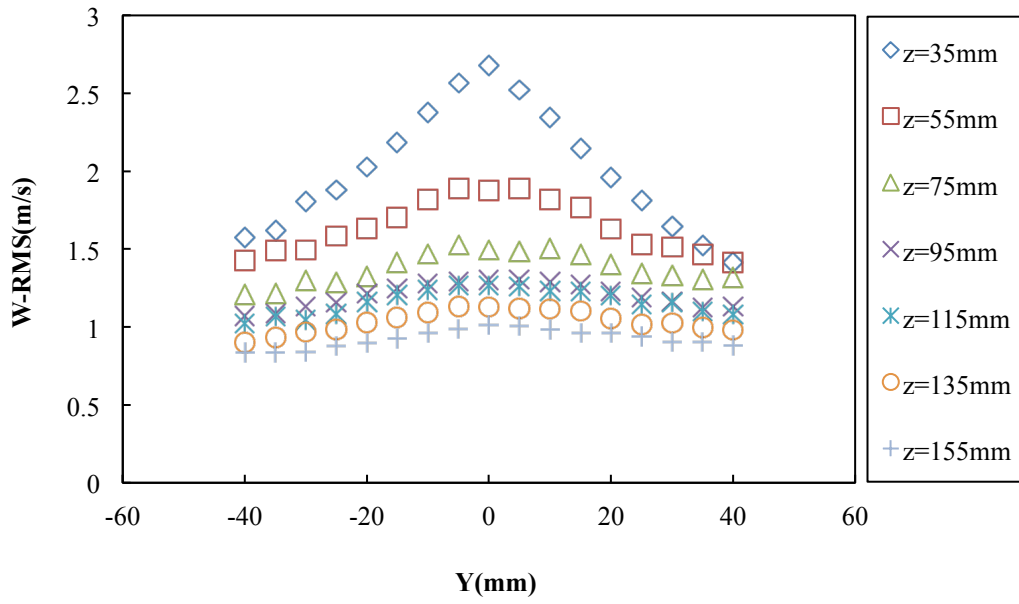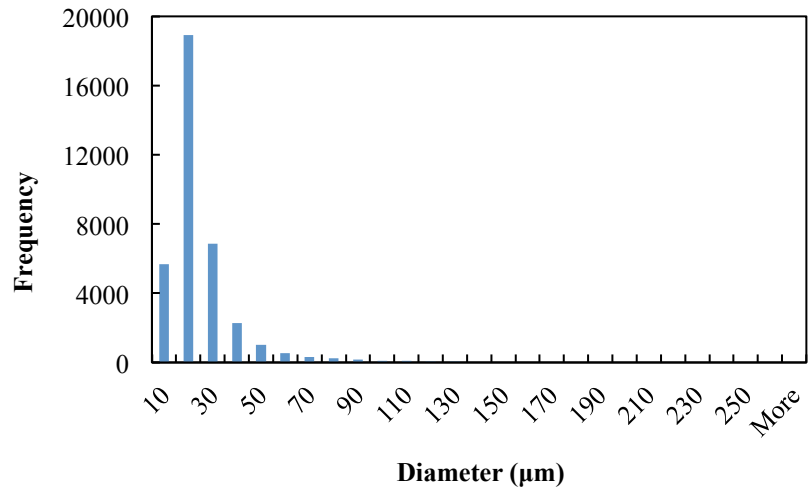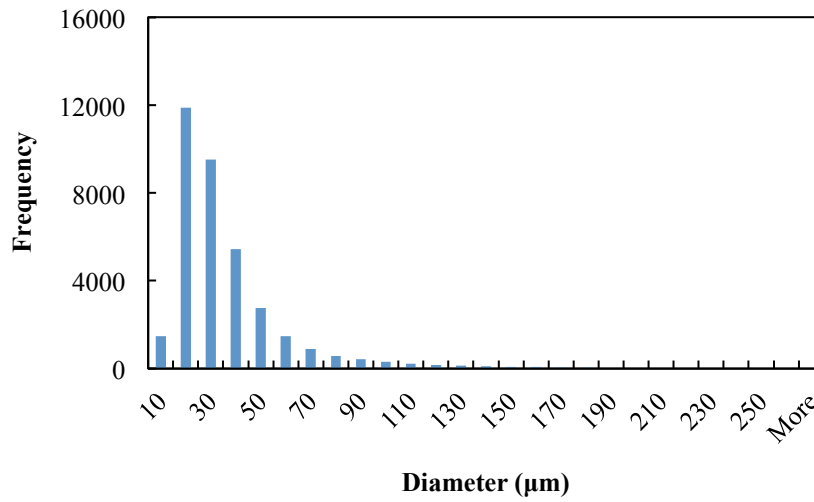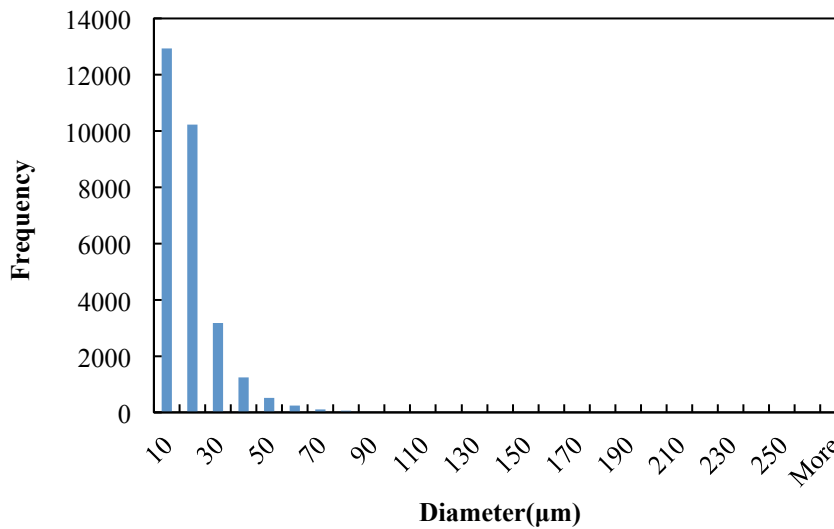
(a)
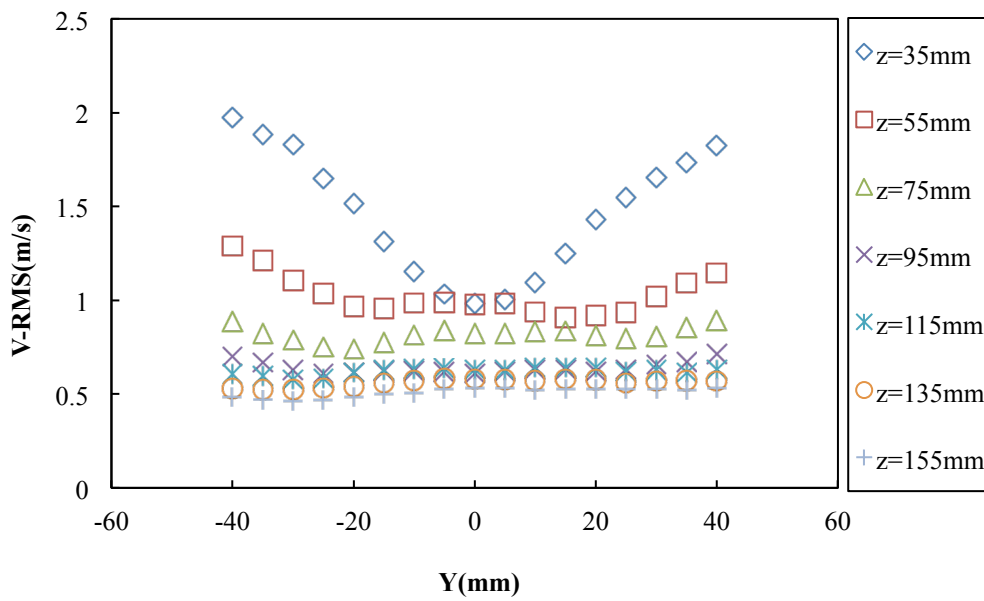
(b)

Fig. 13 Distribution of the RMS of velocity fluctuations for Q_L = 175 mL/min and $\dot{m}_g$ = 11.4 g/min: (a) axial; (b) radial.
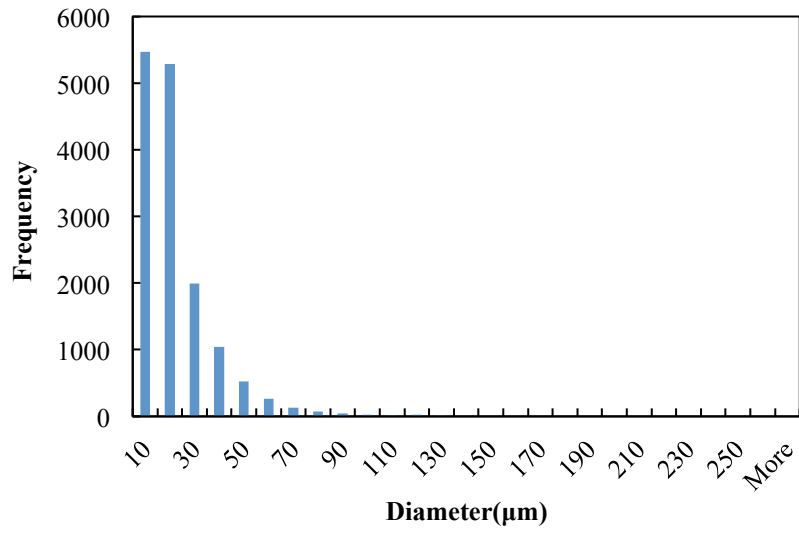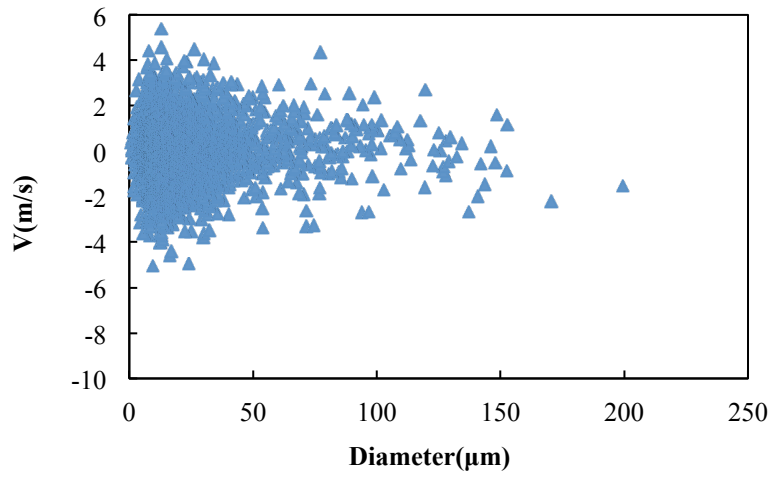
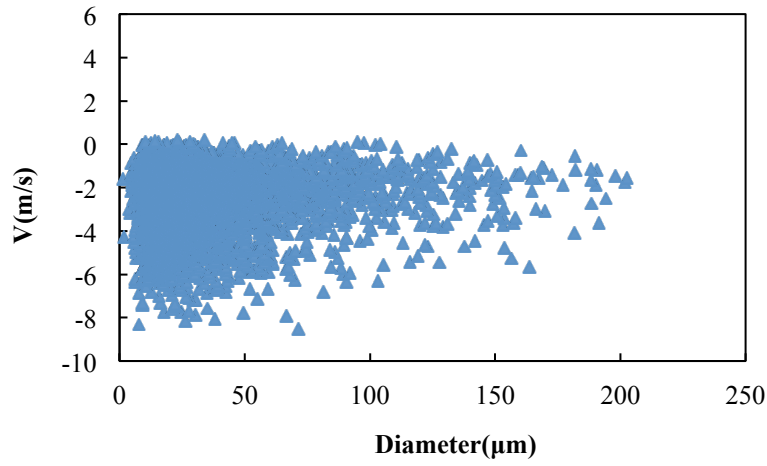(a) Z=35mm, Y = 0 mm

(b) Z=35mm, Y = 25 mm

(c) Z=75mm, Y = 0 mm

(d) Z=75mm, Y = 25 mm

Fig.14. Droplet size histograms for Q_L = 175 mL/min and $\dot{m}_g$ = 11.4 g/min (a) Z=35mm, Y = 0 mm; (b) Z=35mm, Y = 25 mm; (c) Z=75mm, Y = 0 mm;(d) Z=75mm, Y = 25 mm

(a) Z=35mm, Y = 0 mm

(b) Z=35mm, Y = 25 mm
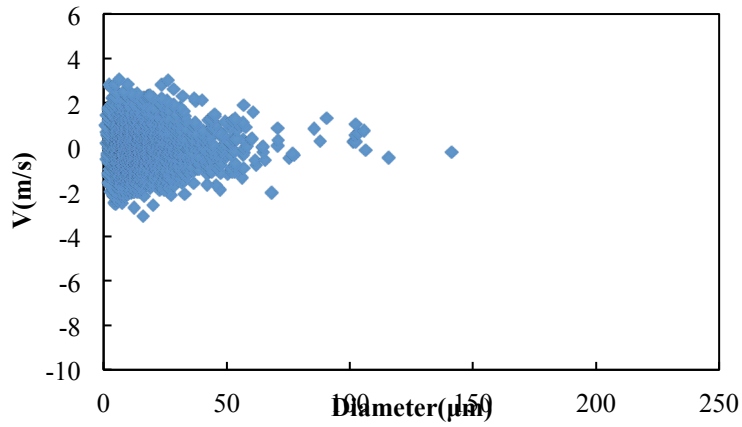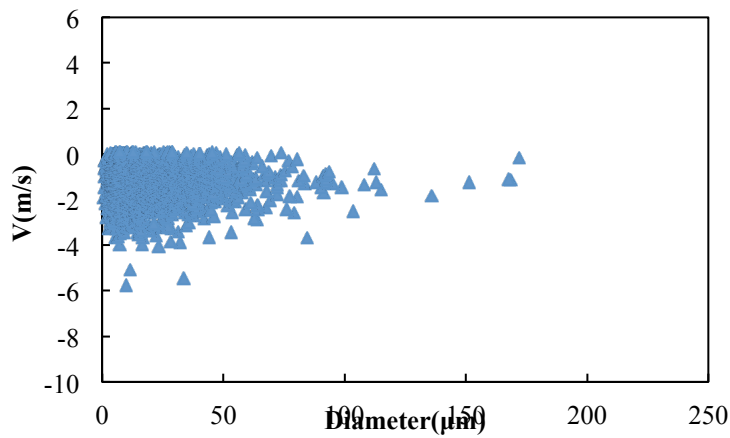
(c) Z=75mm, Y = 0 mm

(d) Z=75mm, Y = 25 mm

Fig.15. Size-velocity correlations for Q_L = 175 mL/min and $\dot{m}_g$ = 11.4 g/min. (a) Z=35mm, Y = 0 mm; (b) Z=35mm, Y = 25 mm; (c) Z=75mm, Y = 0 mm;(d) Z=75mm, Y = 25 mm

- **Effect of water flowrates**

The effect of the water flowrates on the spray is investigated by conducting measurements along the Y-axis at Z = 75 mm on the X = 0 mm plane for $\dot{m}_g$ = 11.4 g/min.

The radial profiles of the droplet D_{32} as a function of the Y position are shown in Fig. 16. Two trends can be distinguished. For Q_L between 100 and 175 mL/min, profiles display a minimum value in the central part at Y = 0 mm (about 38μm) while, away from the central part, D_{32} increases monotonically towards the edge of the spray to about 100 μm at Y = 40 mm. When Q_L reaches 200 mL, the profile starts to flatten and, for higher flowrates, displays a different behavior with maxima at the central part that decreases to lower values as Y increases up to higher values part while at Q_L = 250 mL/min. This is because, for Q_L less than 175 mL/min, the air jet is able to break the water jet completely, and water in the central part experiences stronger interaction, which gives rise to smaller droplets. Larger droplets are dispersed outwards by the air and water impingement. At higher flowrates, Q_L > 175 mL/min, the air jet is not sufficient to break the water jet into small droplets completely, but shear the water from the outside liquid surface, which results in the presence of larger droplets inside the spray center. This can also be inferred from the velocity profiles given in Fig. 17. Therefore, for $\dot{m}_g$ = 11.4 g/min, higher water flowrates lead to relatively poor atomization and mixing in the spray central region, which causes the observed trends of the droplet size radial profile.
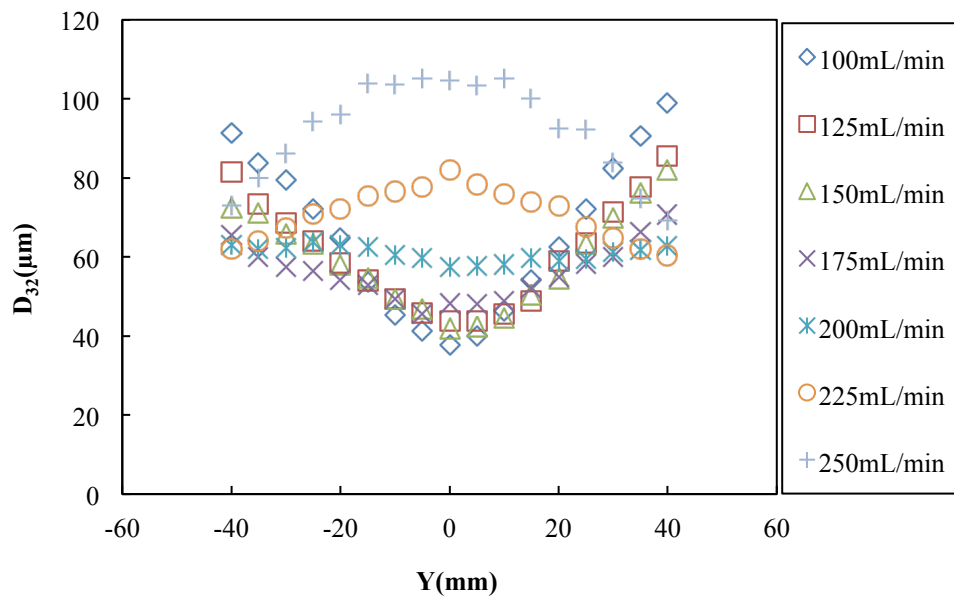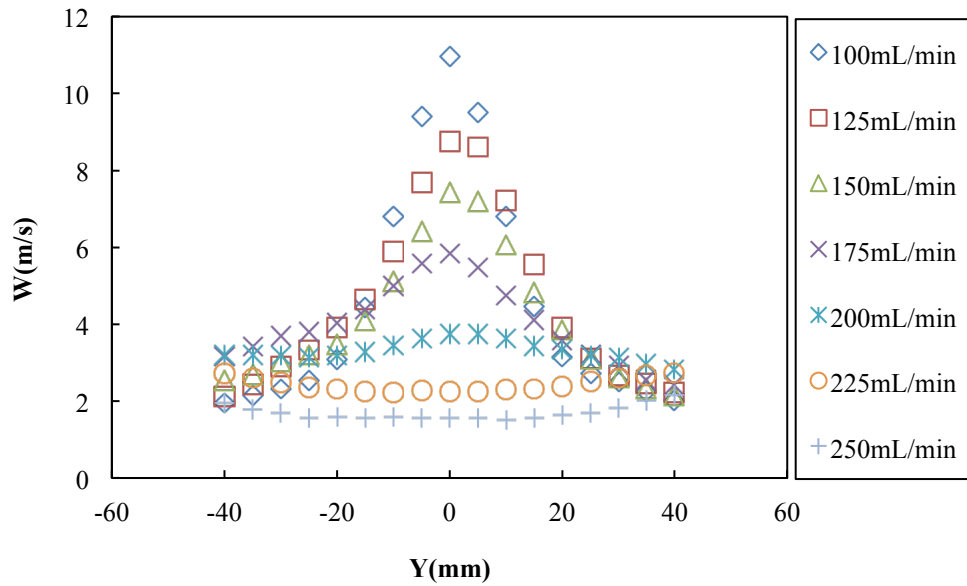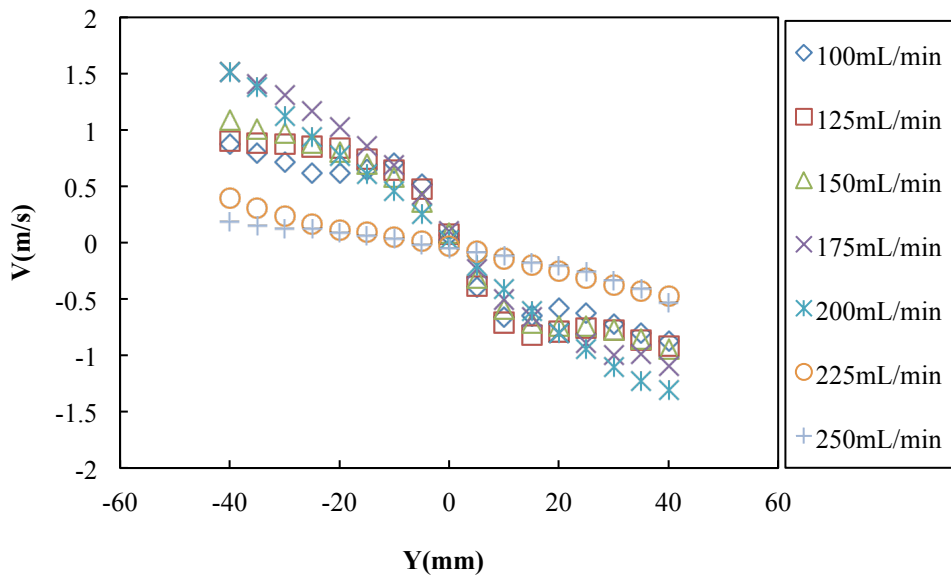

Fig. 16. Effect of water flowrates on droplet size distribution along Y-axis
at Z = 75 mm and $\dot{m}_g$ = 11.4 g/min

(a)

(b)

Fig. 17. Effect of Q_L on droplet velocity distribution along the Y-axis at Z= 75 mm and $\dot{m}_g$ = 11.4 g/min
(a): W; (b): V

Axial and radial mean velocity distributions at Z = 75 mm along the Y-axis are shown in Fig. 17 for different water flowrates. The axial profiles are strongly modulated by the air jet velocity profile for water flowrates below 200 mL/min with a typical bell shaped profile. This is because at a lower water flowrate the water jets do not impinge and interact individually with the air jet to generate small droplets, which are more likely to be entrained and accelerated quickly by the air flow. However, at the edge of the spray, the difference between velocities for different

water flowrates is negligible. For higher liquid flowrates, the profiles are almost flat and not influenced by the air jet. The radial velocity is zero at the spray center at Y = 0 mm, as expected, and on the two sides of the Z-axis of the spray, the velocities have the same magnitude but opposite directions, which demonstrates the accuracy of the alignment of the jet axes during the setup of the experiment.
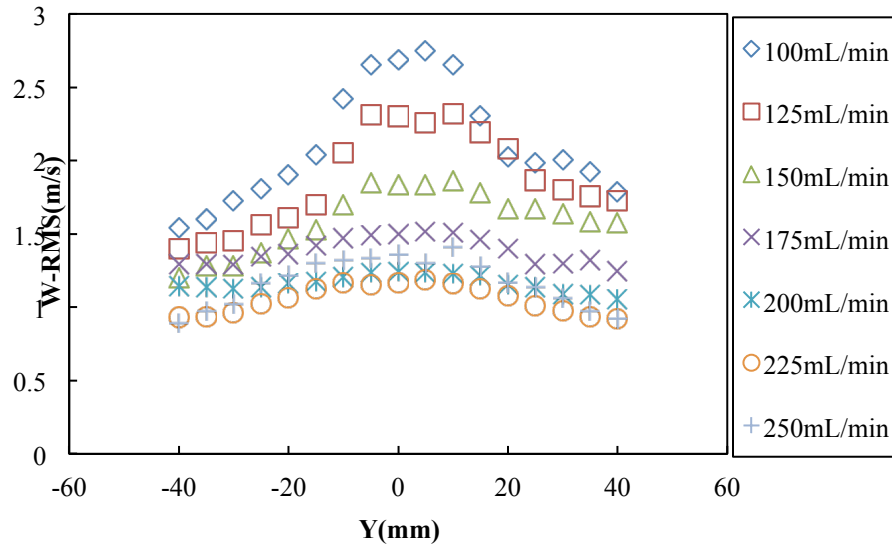
(a)
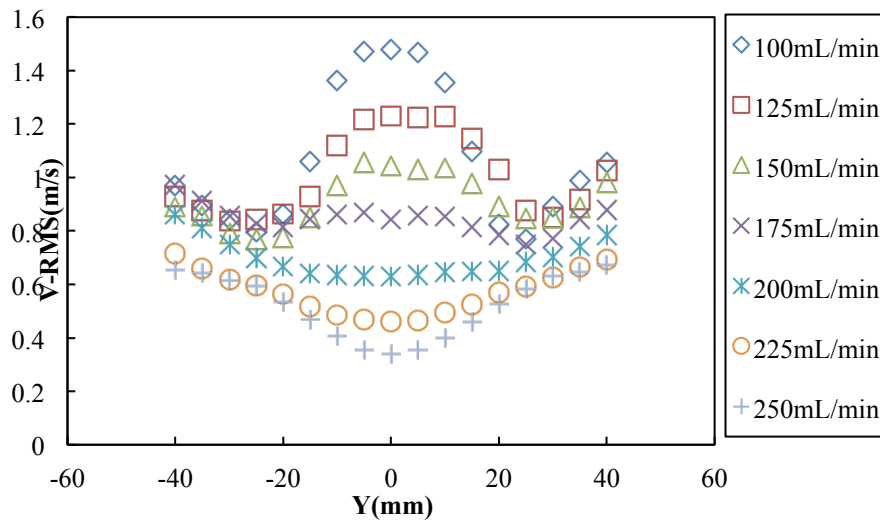
(b)

Fig. 18. Effect of Q_L on the distribution of the RMS of the droplet velocity fluctuations at Z = 75 mm and $\dot{m}_g$ = 11.4 g/min (a): W-RMS; (b): V-RMS

Fig. 18 shows the root mean square of the velocity fluctuations for both axial and radial components. W-RMS is larger at low water flowrates. V-RMS is also larger at small water flowrates, but with a different changing trend from the W-RMS, which also varies for different

28

water flowrates. The RMS V or W of the velocity fluctuations increases significantly close to the axis of the spray for low water flowrates, while the RMS of the velocity fluctuations is reduced for large water flowrates. This qualitative change occurs due to the change of the liquid breakup process. For low water flowrates, the liquid jets do not impinge on each other and generate droplets due to the interaction with the air flow only. For high water flowrates, the interacting liquid jets form a liquid sheet, which then breaks to form droplets with different velocity characteristics. Due to the two reasons mentioned above, the RMS of the velocity fluctuations changes with the water flowrate. Fig. 16 verifies the change of the droplet sizes that are present at the spray axis as the water flowrate increases and support the first reason. The fan-spreading effect is still present due to the inertia of the large droplets, which are generated at different locations during the liquid breakup process for small and large water flowrates.

The effect of water flowrates on the D_{32} distribution along the Z-axis is shown in Fig. 19 for a range of water flowrates. As shown in Fig. 19, for all water flowrates one can distinguish two zones, namely a near field zone, where D_{32} drops to a minimum value at an approximate distance of about $Z = 70$ mm, and an outer zone, beyond around 70 mm, where D_{32} increases again in an almost linear fashion towards the edges of the spray. This further increase may be due to droplet coalescence or a preferential dispersion of different droplet sizes at the location of the droplet formation.
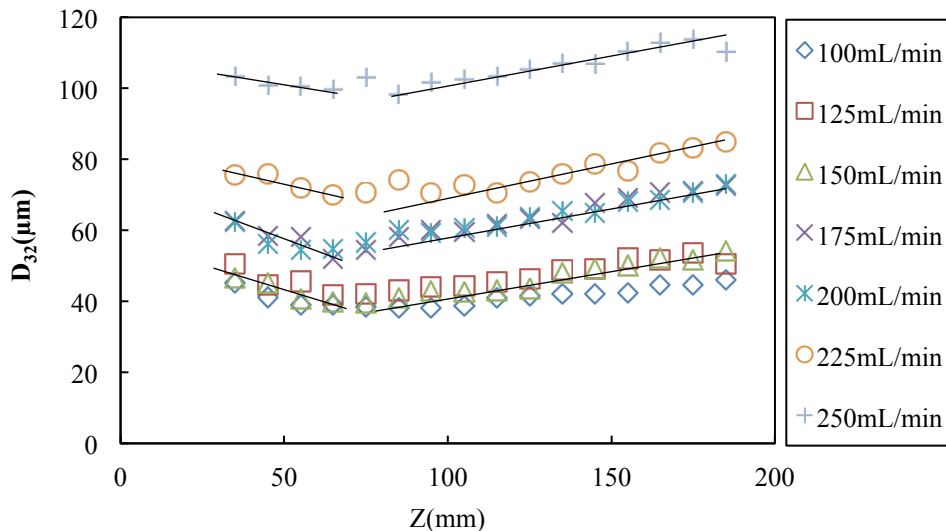

Fig. 19. Effect of water flowrates on droplet size distribution along the spray Z-axis for $\dot{m}_g = 11.4$ g/min (Lines are for visual effect only)

- **Effect of air mass flowrates**

The effect of air mass flowrates on D_{32} distribution of droplets along the spray axis are investigated at $Q_L = 175$ mL/min for three air mass flowrates of 11.4, 17.1 and 22.8 g/min. In Fig.20, one can distinguish two zones and $Z = 70$ mm with a boundary point at around $Z = 70$ mm, where D_{32} reaches the minimum value of around 50, 35 and 30 μm respectively for the three air mass flowrates displayed on the figure.
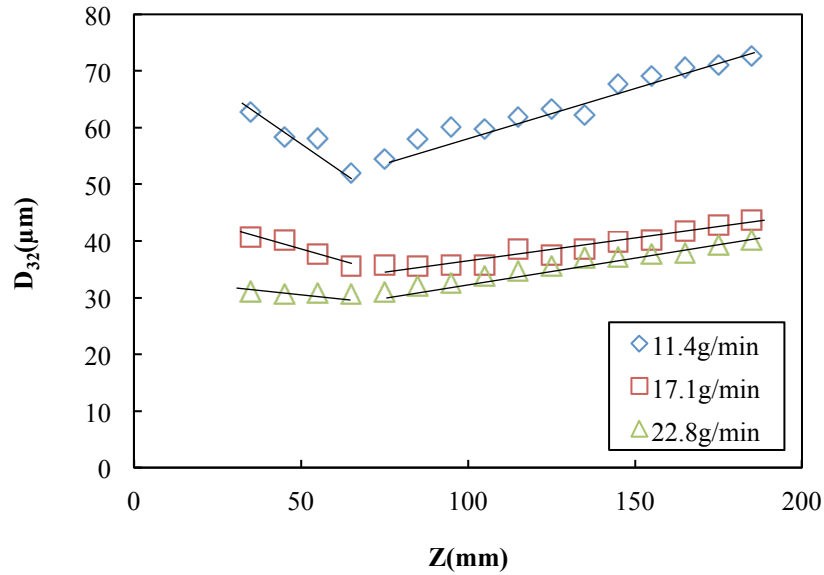

Fig. 20. Effect of $\dot{m}_g$ on droplet size distribution along the spray Z-axis, Q_L=175 mL/min. (Lines are for visual effect only)

Beyond $Z = 70$ mm, D_{32} along the spray axis increases slightly with the increasing distance from the impingement point possibly due to the droplet coalescence or preferential dispersion of different droplet sizes during breakup. The effects of increasing air mass flowrates on D_{32} become less significant when the air mass flowrate reaches a certain value, as shown in Fig. 20, from $\dot{m}_g = 11.4$ to $\dot{m}_g = 17.1$ g/min D_{32} decreases by 20 μm, while from $\dot{m}_g = 17.1$ to $\dot{m}_g = 11.4$ g/min, the decrease is only about 5 μm.

3.3 Turbulent kinetic energy of droplets

Turbulent kinetic energy (TKE) is calculated based on the estimation correlation adopted by [25]:

$$k = 0.75(\overline{u_z'^2} + \overline{u_y'^2})$$ (4)

where, u_z' and u_y' are fluctuating droplet velocities in axial and radial direction.

     Fig. 21 displays the TKE distribution at Z = 75 mm along the Y-axis at different water flowrates. It is symmetrical around Y = 0 mm. The distribution is consistent with the root mean square of the velocity fluctuations, which indicates stronger interaction in the spray central region, while the interaction weakens with increasing water flowrates.

     Fig. 22 shows the spatial distribution on the plane of X = 0 mm at different Z positions, and TKE decreases from 6 to about 0.5 with the increasing axial distance. Thus, TKE is larger at a lower water flowrate at positions near the impingement zone. One can see that larger TKE benefits the atomization and results in faster liquid jet breakup.
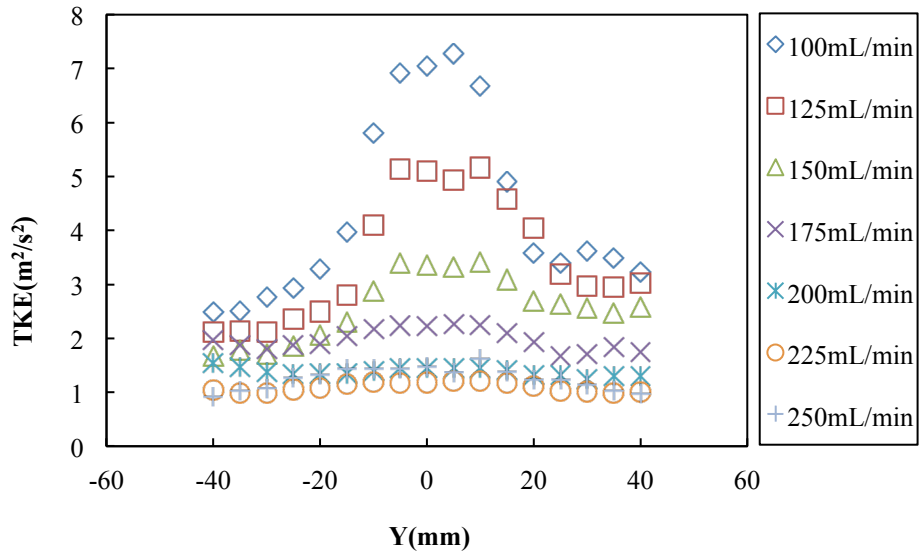

Fig. 21. TKE distribution at Z = 75 mm and $\dot{m}_g$ = 11.4 g/min for various water flowrates
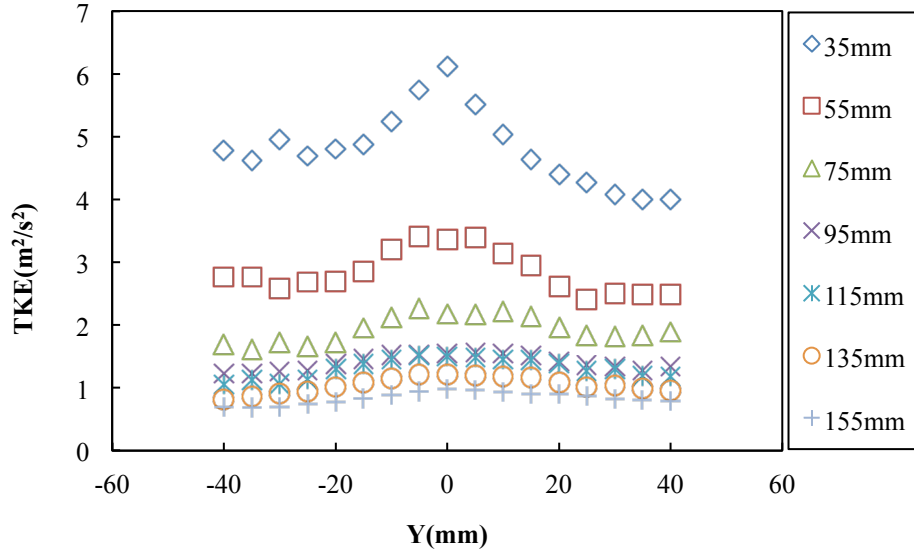
Fig. 22. TKE spatial distribution for $\dot{m}_g = 11.4$ g/min and $Q_L = 175$ mL/min

4. Conclusions

The flow characteristics of two opposed horizontal impinging water jets in the absence and presence of an impinging air jet were investigated. Flow visualization and measurements of droplet size, velocity and RMS of the velocity fluctuations were conducted at several water and air flowrates.

Without the air jet, a circular water sheet is generated in the vertical plane, of which the diameter increases linearly with the water jet Reynolds number and Weber number in agreement with previous findings. The average diameter of droplets shed from edge of the water sheet decreases with increasing Weber number scaled with density ratio. The air jet is found to affect significantly liquid jets atomization. With the increase of air flow rate, the circular water sheet disappears, large ligaments generates, followed by small droplets and improved atomization.

PDA measurements at $\dot{m}_g = 11.4$ g/min show that D_{32} at the spray center is the smallest (around 38µm) for $100 < Q_L < 175$ mL/min and increases towards the spray edges. Further increase in the water flow rate leads to relative large droplets, axial velocity and RMS of velocity fluctuations, i.e., the increase of water flowrates leads to poor atomization in the central part.

The spatial distribution of D_{32} for $Q_L = 175$ mL/min at $\dot{m}_g = 11.4$ g/min demonstrates that the smallest droplets (around 50 µm) exist in the region about 65 mm to 85 mm downstream below the impingement point in the central region. Axial velocity W, RMS of velocity

32

fluctuations and droplet TKE are larger at positions closer to the impingement point and decrease outwards and downstream due to the decay of air jet momentum.

The D_{32} of droplets along the spray Z-axis decreases from the $Z = 35$ mm to 75 mm due to breakup from the interaction between water and air jets, and then increased slightly possibly due to droplet coalescence or preferential dispersion of different droplet sizes. In addition, D_{32} becomes smaller with the increase of air mass flowrate within the range of the current study.

Comparison of the variation of non-dimensional Sauter mean diameter D_{32}/d plotted against the ALMR between the current study and that obtained at a 90° impinging angle of the liquid jets indicates better atomization for the current configuration.

Acknowledgements

References

[1]   G. P. Sutton and D. M. Ross, "Rocket Propulsion Elements, An Introduction to The Engineering of Rockets, 4h ed," ed: John Wiley and Sons, New York, 1976.
[2]   M. Icardi, E. Gavi, D. L. Marchisio, A. A. Barresi, M. G. Olsen, R. O. Fox, et al., "Investigation of the flow field in a three-dimensional confined impinging jets reactor by means of microPIV and DNS," Chemical engineering journal, vol. 166, pp. 294-305, 2011.
[3]   A. Lefebvre, Atomization and sprays vol. 1040: CRC press, 1988.
[4]   L. Bayvel, Liquid atomization vol. 1040: CRC Press, 1993.
[5]   F. Bai, H. Diao, M. Zhang, Q. Chang, E. Wang, and Q. Du, "Breakup characteristics of power-law liquid sheets formed by two impinging jets," Fluid Dynamics Research, vol. 46, p. 055506, 2014.
[6]   F. Savart, "Mémoire sur la constitution des veines liquides lancées par des orifices circulaires en mince paroi," Ann. Chim. Phys, vol. 53, p. 1833, 1833.
[7]   J. W. Bush and A. E. Hasha, "On the collision of laminar jets: fluid chains and fishbones," Journal of fluid mechanics, vol. 511, pp. 285-310, 2004.
[8]   R. Li and N. Ashgriz, "Characteristics of liquid sheets formed by two impinging jets," Physics of fluids, vol. 18, p. 087104, 2006.
[9]   G. Bailardi, M. Negri, and H. Ciezki, "Several aspects of the atomization behavior of various Newtonian fluids with a likeon-like impinging jet injector," in Proc. 23rd European Conf. on Liquid Atomization and Spray Systems, Brno, Czech Republics, 2010.
[10]   J. Zhang, Y. Liu, G. Qi, W. Jiao, and Z. Yuan, "Flow characteristics in free impinging jet reactor by particle image velocimetry (PIV) investigation," Fluid Dynamics Research, vol. 48, p. 045505, 2016.
[11]   V. Young, Liquid Rocket Engine Combustion Instability vol. 169: AIAA, 1995.

[12]   N. Ashgriz, "Impinging jet atomization," Handbook of Atomization and Sprays, ed: Springer, , pp. 685-707, 2011.

[13]   C. Indiana, M. Bellenoue, and B. Boust, "Experimental Investigations of Drop Size Distributions with Impinging Liquid Jets Using Phase Doppler Anemometer," International Journal of Energetic Materials and Chemical Propulsion, vol. 14, 2015.

[14]   N. Bremond and E. Villermaux, "Atomization by jet impact," Journal of Fluid Mechanics, vol. 549, pp. 273-306, 2006.

[15]   G. Baek, S. Kim, J. Han, and C. Kim, "Atomization characteristics of impinging jets of gel material containing nanoparticles," Journal of Non-Newtonian Fluid Mechanics, vol. 166, pp. 1272-1285, 2011.

[16]   M. Negri, H. Ciezki, and S. Schlechtriem, "Spray behavior of non-newtonian fluids: correlation between rheological measurements and droplets/threads formation," Progress in Propulsion Physics, vol. 4, pp. 271-290, 2013

[17]   J. Huang, "The break-up of axisymmetric liquid sheets," Journal of Fluid Mechanics, vol. 43, pp. 305-319, 1970.

[18]   E. Villermaux and C. Clanet, "Life of a flapping liquid sheet," Journal of fluid mechanics, vol. 462, pp. 341-363, 2002.

[19]   C. Clanet and E. Villermaux, "Life of a smooth liquid sheet," Journal of fluid mechanics, vol. 462, pp. 307-340, 2002.

[20]   G. Coppola and A. Gomez, "Experimental study of highly turbulent isothermal opposed-jet flows," Physics of fluids, vol. 22, p. 105101, 2010.

[21]   J. Zhang, J. Yan, X. Dong, P. Shang, and Y. Feng, "Experimental study on turbulence properties in the dual nozzle opposed impinging stream mixer," The Canadian Journal of Chemical Engineering, vol. 95, pp. 550-558, 2017.

[22]   J. Li, H. Wang, Y. Xiong, G. Jiang, Z. Liu, and C. Zheng, "Experimental investigation on turbulence modification in a dilute gas-particle axisymmetric opposed jets flow," Chemical Engineering Journal, vol. 286, pp. 76-90, 2016.

[23]   W. F. Li, T. L. Yao, and F. C. Wang, "Study on factors influencing stagnation point offset of turbulent opposed jets," AIChE journal, vol. 56, pp. 2513-2522, 2010.

[24]   D. Wu, J. Li, Z. Liu, Y. Xiong, C. Zheng, and P. R. Medwell, "Eulerian and Lagrangian stagnation plane behavior of moderate Reynolds number round opposed-jets flow," Computers & Fluids, vol. 133, pp. 116-128, 2016.

[25]   J. Zhang, Y. Liu, and Y. Luo, "The turbulent behavior of novel free triple-impinging jets with large jet spacing by means of particle image velocimetry," Chinese Journal of Chemical Engineering, vol. 24, pp. 757-766, 2016.

[26]   M. M. Avulapati and R. R. Venkata, "Experimental studies on air-assisted impinging jet atomization," International Journal of Multiphase Flow, vol. 57, pp. 88-101, 2013.

[27]   Y. Xia, L. Khezzar, M. Alshehhi, and Y. Hardalupas, "Droplet size and velocity characteristics of water-air impinging jet atomizer," International Journal of Multiphase Flow, vol. 94, pp. 31-43, 2017.

[28]   C. A. Schneider, W. S. Rasband, and K. W. Eliceiri, "NIH Image to ImageJ: 25 years of image analysis," Nature methods, vol. 9, p. 671, 2012.

[29]   T. J. Collins, "ImageJ for microscopy," Biotechniques, vol. 43, pp. 25-30, 2007.

[30]   B. P. Husted, P. Petersson, I. Lund, and G. Holmstedt, "Comparison of PIV and PDA droplet velocity measurement techniques on two high-pressure water mist nozzles," Fire safety journal, vol. 44, pp. 1030-1045, 2009.

[31]   W. Lai, J. Shakal, and D. Troolin, "Accuracy, Resolution, and Repeatability of Powersight PDPA and LDV Systems," TSI Technical Note P, p. A4, 2013.

[32] C. Clanet, "Waterbells and liquid sheets," Annu. Rev. Fluid Mech., vol. 39, pp. 469-496, 2007.

[33] G. Faeth, L.-P. Hsiang, and P.-K. Wu, "Structure and breakup properties of sprays," *International Journal of Multiphase Flow,* vol. 21, pp. 99-127, 1995.

[34] J. C. Boden, Hardalupas, Y. Krenteras, P. Taylor A.M.K.P., "Spray characteristics from free impinging air and liquid jets", Proc. 15th ILASS-Europe 99, Toulouse, July 5-7,1999.

[35] Y. Hardalupas, A. Taylor, and J. Whitelaw, "Velocity and particle-flux characteristics of trubulent particle-laden jets," in Proceedings of the Royal Society of London A: Mathematical, Physical and Engineering Sciences, 1989, pp. 31-78.

[36] Y. Hardalupas, A. Taylor, and J. Whitelaw, "Velocity and size characteristics of liquid-fuelled flames stabilized by a swirl burner," in Proceedings of the Royal Society of London A: Mathematical, Physical and Engineering Sciences, 1990, pp. 129-155.